Chinese Chemical Letters 32 (2021) 3245–3251

Contents lists available at ScienceDirect

Chinese Chemical Letters

journal homepage: www.elsevier.com/locate/cclet

Communication

Magnetic rod-based metal-organic framework metal composite as multifunctional nanostirrer with adsorptive, peroxidase-like and catalytic properties

Benjamin Edem Meteku[a,b,1], Jiankun Huang[a,1], Jingbin Zeng[a,*], Sobia Aslam[c], Yu Zhang[b], Xue Zhang[a], Bingwen Cui[a], Cong-ying Wen[a], Zifeng Yan[a,b,*]

[a] College of Science and State Key Laboratory of Heavy Oil Processing, China University of Petroleum (East China), Qingdao 266580, China
[b] College of Chemical Engineering, China University of Petroleum (East China), Qingdao 266580, China
[c] Department of Chemistry, Abdul Wali Khan University, Mardan 23200, Pakistan

ARTICLE INFO

Article history:
Received 14 January 2021
Received in revised form 15 February 2021
Accepted 22 February 2021
Available online 9 March 2021

Keywords:
Nanostirrer
Nanozyme
Magnetic field
MOF
Adsorption
Catalysis

ABSTRACT

Although magnetic stirring is frequently used to enhance the kinetics for adsorption, chemical and biochemical reactions, the introduction of stirrers inevitably leads to the adsorption of analytes and thus interferes with the efficiency of the chemical process or reaction. In this work, magnetic Fe_3O_4 nanorods with tunable length-to-diameter ratio were synthesized *via* a hydrothermal method and used as templates for the *in-situ* depositing of MIL-100(Fe) and gold nanoparticles. Such nanorod-based material can not only function as an adsorbent, nanozyme, and a heterogeneous catalyst for corresponding applications but also serve as a magnetic nanostirrer to enhance kinetics. As a proof-of-concept, the capture of bacteria pathogen, mimic-peroxidase-based colorimetric detection of hydrogen peroxide, and the catalytic reduction of selected organic pollutants were conducted using the as-synthesized Fe_3O_4@MIL-100(Fe)-Au nanostirrer with and without magnetic field. The results show that the rates of bacteria capture, mimetic enzyme reaction and catalysis were tremendously expedited. We believe this magnetic field-assisted approach holds great promise for future applications, because, not only does it eliminate the use of external magnetic stirrers and thereby decrease the risk of foreign pollution but also, is adaptable for nanoscale reaction systems where conventional stirring is not applicable due to size limitations.

Research advance in the field of nanoscience has led to the development of auspicious multifunctional materials that were inconceivable some decades ago. Some of these materials are obtained by integrating two or more functional materials into a composite, unequaled in performance and properties by the individual components [1–3]. A typical example is the integration of magnetic nanoparticles with metal-organic frameworks (MOFs) and noble metals.

In recent times, magnetic nanoparticles have gained considerable attention in various fields of research not only because of their unique size (1–100 nm) and extraordinary surface areas but also due to their superparamagnetic properties and biocompatibility as in the case of Fe_3O_4 [4,5]. Among the magnetic nanoparticles (Fe, Co, Ni, and recently Ru [6]), iron-based magnetic materials, especially Fe_3O_4 have been at the forefront of most applications [7]. However, Fe_3O_4 nanorod which has some reported advantages over other shapes such as nanosphere has received less attention in terms of research output [8].

MOFs, a class of crystalline polymeric materials consisting of metal ions (or clusters) linked by organic ligand, have remarkable properties such as ultrahigh surface area, tunable pore size, thermal stability, ordered structure among others [6,9]. As a result of these unparalleled properties, they have been touted for a broad spectrum of applications including; catalysis, gas storage and separation, energy storage, adsorption, environmental remediation, biomedicine, *etc.* [10–13].

Noble metal nanoparticles are an important class of metals that are desired for several applications due to their high resistance to oxidation, optical, mechanical, and catalytic properties [14]. However, due to their high surface energies, noble metal

* Corresponding authors at: College of Science and State Key Laboratory of Heavy Oil Processing, China University of Petroleum (East China), Qingdao 266580, China.
E-mail addresses: xmuzjb@163.com (J. Zeng), zfyancat@upc.edu.cn (Z. Yan).
[1] These authors contributed equally to this work.

https://doi.org/10.1016/j.cclet.2021.03.019

nanoparticles tend to be thermodynamically unstable and hence their propensity to aggregate which adversely affects their applications such as in catalysis. An innovative way of offsetting this deficiency is by immobilizing noble metal nanoparticles in metal-organic framework. Such an intervention will render it useful for several applications [15].

Effective mixing is crucial for achieving faster adsorption kinetics and chemical reaction. Therefore, to promote rapid mixing and effectively enhance kinetics, reaction mixtures are agitated on laboratory shakers or stirred with mechanical stirrers, magnetic stir bars, *etc.* depending on the reaction conditions [16]. However, most conventional stirring systems are impractical for microscale-nanoscale reaction systems such as microliter bioassay, micro-droplets, and other classical lab-on-chip applications [17]. There is therefore the need for the development of effective stirring systems for such applications. Also, for typical conventional stirring systems, the stirring process may lead to some degree of loss in the reactant species and catalyst (for catalytic reactions) due to the adsorption of the reactant species on the stirring device and consequentially affect the generated products [18]. Furthermore, incontrovertible proof in recent studies suggests that the surface of magnetic stir bars are susceptible to microscale destruction resulting in defects that trap trace amounts of metals such as Au, Pd, Pt, Fe from reaction mixtures [19]. Conventional cleaning processes may not necessarily suffice to eliminate these trapped metal species and hence these trapped metal impurities inadvertently have a significant impact on the rate of chemical reaction [20]. Notwithstanding these drawbacks, conventional stirrers are still vastly used in chemical reactions. Inspired by the synergistic effect in the properties of composite materials, we propose the encapsulation of magnetic nanomaterials in MOFs and subsequently immobilize noble metals on the magnetic MOF structure to form a unique triad-composite material with plausible outstanding adsorptive and catalytic properties and potential for stirring chemical reactions especially microscale reaction systems. On this premise, we set out to explore the synthesis and application of Fe_3O_4@MIL-100(Fe)-Au for bacteria pathogen adsorption, colorimetric detection of H_2O_2 and catalytic reduction of selected organic pollutants on a magnetic field.

The magnetic composite, Fe_3O_4@MIL-100(Fe)-Au was synthesized using Fe_3O_4 nanorods, MIL-100 (Fe), and Au nanoparticles. As shown in Fig. 1, Fe_3O_4 nanorod, the source of the magnetic property, is obtained *via* the reduction of β-FeOOH. Not only does it function as the source of magnetic property for achieving stirring and enhance adsorption but also functions as both a promoter to enhance catalysis on a magnetic field and to conveniently effect separation of nanostirrer from the reaction stream. The MOF, MIL-100(Fe) provides the needed surface area and support for the active component, Au to be attached. As a proof-of-concept, the adsorption of bacteria pathogen from solution was explored. Catalysis, another important industrial process was explored [21]. The composite was applied as a nanozyme for the colorimetric detection of H_2O_2 in the presence and absence of a magnetic field. In addition, the reduction of 4-nitrophenol (4-NP) at the presence of $NaBH_4$ to 4-aminophenol (4-AP), an important chemical intermediate used in the manufacture of antipyretic drugs was chosen as the model reaction for testing the catalytic behavior of the synthesized composite. The role of the magnetic property in enhancing catalysis was elucidated by comparing magnetic field-assisted catalysis with a stationary catalysis system (non-magnetic field-assisted system). To further corroborate the pollutant reduction prowess of the composite and the effect of the magnetic property on catalysis, two other cationic dyes methylene blue (MB) and rhodamine B (RhB) were explored.

Rod-shaped β-FeOOH, the base material for magnetite was successfully produced from CTAB-assisted hydrolysis of $FeCl_3{\cdot}6H_2O$ as shown in the transmission electron microscopy (TEM) image in Fig. 2a. When nanocrystals undergo chemical transformations such as reduction at high temperature (240 °C), mechanical deformations and structural collapse often occur [22].

To obviate this occurrence, the capping ligand polyacrylic acid (PAA) was used to preserve the morphology of nanorods. The successful reduction of β-FeOOH *via* the surface protection strategy resulted in the formation of magnetic Fe_3O_4 nanorod (Fig. 2b). The cogent role of PAA in the preservation of the morphology of the nanorod during the reduction process was explored by direct reduction of β-FeOOH to form Fe_3O_4 without surface modification with PAA. Although a magnetic product was formed, the TEM image (Fig. S1 in Supporting information) reveals a total collapse of the rod shape. Fig. 2c confirms the formation of Fe_3O_4@MIL-100(Fe) core-shell structure *via* the layer-by-layer approach. Finally, the successful deposition of Au nanoparticles on Fe_3O_4@MIL-100(Fe) to form the unique magnetic rod-based triad-composite, Fe_3O_4@MIL-100 (Fe)-Au as shown in Fig. 2d. The elemental analysis of the synthesized composite confirms the formation of Fe_3O_4@MIL-100(Fe)-Au. As shown in the high-angle annular dark-field scanning transmission electron microscopy (HAADF- STEM) image in Fig. 2e and the corresponding elemental mapping in Fig. 2f, the presence of Au, Fe, C, and O, the main elemental composition of the catalyst affirms this assertion.

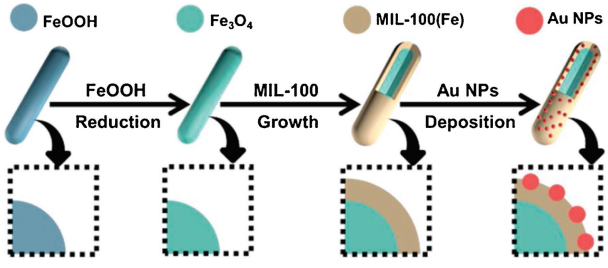

Fig. 1. Schematic illustration of the synthesis methodology for Fe_3O_4@MIL-100(Fe)-Au.

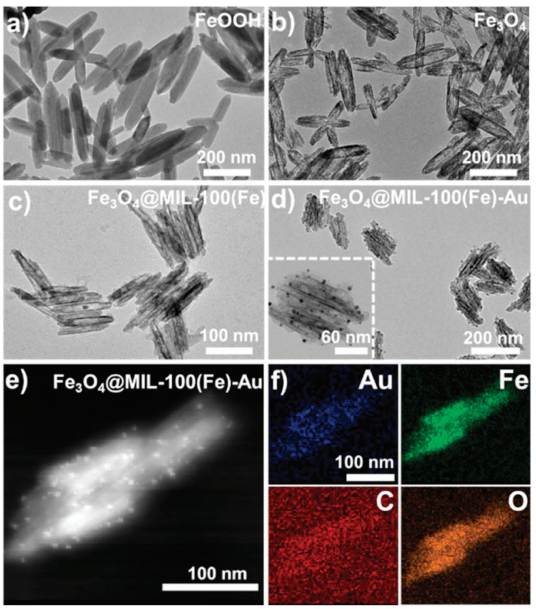

Fig. 2. TEM images of (a) β-FeOOH, (b) Fe_3O_4, (c) Fe_3O_4@MIL-100(Fe) and (d) Fe_3O_4@MIL-100(Fe)-Au. (e) STEM-HAADF image of Fe_3O_4@MIL-100(Fe)-Au.(f) Elemental mapping results of Fe_3O_4@MIL-100(Fe)-Au.

Powder X-ray diffraction (XRD) patterns were used to determine the chemical composition and crystal phases of materials at various stages of the synthesis and confirm the formation of β-FeOOH, Fe_3O_4, Fe_3O_4@MIL-100(Fe), and Fe_3O_4@MIL-100(Fe)-Au as summarized in Fig. 3a. As detailed in Fig. S2a (Supporting information), the XRD pattern of the obtained product after hydrolysis demonstrates the formation of the tetragonal phase of β-FeOOH owing to the presence of peaks that can be indexed to β-FeOOH (JCPDS No. 75-1594). Similar observations of XRD patterns for β-FeOOH was made elsewhere [8]. The conversion of β-FeOOH to Fe_3O_4 was confirmed by the XRD pattern in Fig. S2b (Supporting information) which is in agreement with JCPDS No. 75-0033 for Fe_3O_4. The formation of MIL-100(Fe) around Fe_3O_4 is confirmed in Fig. S2c (Supporting information) and is in accord with similar observations in literature [23]. The successful deposition of Au on the magnetic MOF to form Fe_3O_4@MIL-100 (Fe)-Au is corroborated by the presence of the characteristic peaks of Au at $2\theta = 38.2°$, 44.4°, 64.6°, and 77.5° corresponding to the lattice planes (111), (200), (220) and (311), respectively (JCPDS No. 04-0784) (Fig. S2d in Supporting information).

The Fourier transform infrared (FTIR) spectra (Fig. S3a in Supporting information) gives further credence to the successful formation of Fe_3O_4@MIL-100(Fe)-Au (blue curve). The presence of strong stretching-vibration bands in the range of 3200–3600 cm^{-1} is characteristic of OH functional group, an indication of the presence of the hydroxyl group in the preparatory stages of Fe_3O_4. The observed band at 569 cm^{-1} can be ascribed to Fe-O stretching vibrations in Fe_3O_4 spectrum as similarly observed in literature [24]. The functionalization of Fe_3O_4 with Mercaptoacetic acid (MAA) to facilitate the growth of MIL-100(Fe) is confirmed by the appearance of bands at 1625 cm^{-1} and 1380 cm^{-1}, typical C=O stretching vibrations of carboxylic acid. The bands at 1550 cm^{-1} and 1437 cm^{-1} can be attributed to C=C stretching vibrations in the benzene ring, a component of trimesic acid, a building block of the MOF. The band at 714 cm^{-1} is attributable to the flexural vibration of C–H benzene ring. Finally, the successful deposition of Au on Fe_3O_4@MIL-100(Fe) was confirmed by the appearance of a new band at 1292 cm^{-1} in the Fe_3O_4@MIL-100 (Fe)-Au spectrum.

Also, ultraviolet-visible spectroscopic studies of the synthesis stages further allude to the formation of β-FeOOH (black curve), Fe_3O_4 (red curve), and Fe_3O_4@MIL-100(Fe) (blue curve) along the synthesis route and the eventual formation of Fe_3O_4@MIL-100(Fe)-Au (pink curve) with the unique absorption band of Au at 533 nm (Fig. S3b in Supporting information).

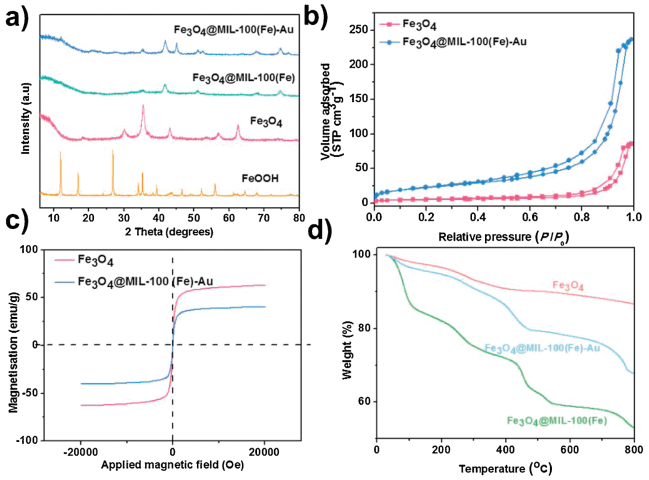

Fig. 3. (a) XRD patterns of β-FeOOH, Fe_3O_4, Fe_3O_4@MIL-100(Fe) and Fe_3O_4@MIL-100(Fe)-Au. (b) N_2 adsorption-desorption isotherm for Fe_3O_4 and Fe_3O_4@MIL-100(Fe)-Au. (c) Magnetic hysteresis loop of Fe_3O_4 and the as-synthesized Fe_3O_4@MIL-100(Fe)-Au. (d) Thermogravimetric analysis curve for Fe_3O_4, Fe_3O_4@MIL-100 (Fe) and Fe_3O_4@MIL-100(Fe)-Au.

The surface area of Fe_3O_4 (red curve) and Fe_3O_4@MIL-100(Fe)-Au (blue curve) was characterized by N_2 adsorption-desorption isotherms as shown in Fig. 3b. The Brunauer-Emmett-Teller (BET) surface area of Fe_3O_4 nanorod was found to be 36.65 m^2/g. Upon the growth of 5-cycles of MOF around the nanorod and the subsequent deposition of Au on the magnetic MOF to form Fe_3O_4@MIL-100(Fe)-Au composite, a BET surface area of 113.83 m^2/g was realized. This is relatively high as compared to the recorded 211 m^2/g for 20-cycles of a similar composite as observed elsewhere [25]. The overall surface area of the composite as recorded above impacts positively on the available active sites to favor catalysis. Furthermore, by dint of the relatively high surface area of the composite, it can exhibit adsorptive tendencies as well.

The magnetic property of the as-synthesized composite was determined at room temperature by vibrating sample magnetometer (VSM) and the corresponding magnetic hysteresis loop presented in Fig. 3c. The magnetization saturation (Ms) values for Fe_3O_4 nanorods and Fe_3O_4@MIL-100 (Fe)-Au were 62.9 emu/g and 40.5 emu/g, respectively. The observed reduction in the magnetic property of the composite to 40.5 emu/g (35.6% reduction) is expected and can be attributed to the presence of the non-magnetic MIL-100(Fe) shell and the noble metal, Au around the magnetic Fe_3O_4 nanorod core. Generally, for magnetic MOF composites, increasing the number of MOF cycles (MOF layer thickness) results in a decrease in the magnetic property of such composites [6]. To avoid too-thick a MOF shell which will be detrimental to the intended use of the magnetic property to enhance catalysis, only 5-cycles of MOF shells were built around the magnetic core. Therefore, on account of this logical trade-off, Fe_3O_4@MIL-100(Fe)-Au exhibited similar superparamagnetic properties as Fe_3O_4. The thermal stability of Fe_3O_4, Fe_3O_4@MIL-100(Fe), and Fe_3O_4@MIL-100(Fe)-Au was evaluated by thermogravimetric analysis (TGA). As illustrated in Fig. 3d above, the thermogram of Fe_3O_4 (red curve) showed an estimated weight loss of 13.42% over the entire analysis period. As evidenced in the thermogram, the weight loss mainly occurred at temperatures below 400 °C and can be attributed to evaporation of water molecules adsorbed on the surface of Fe_3O_4 and volatilization of unreacted precursors during the synthesis. The thermogram of Fe_3O_4@MIL-100(Fe) (green curve) showed an estimated 47.10% weight loss over the analysis period and gives credence the successful growth of MOF around the magnetic core. The observed weight loss can be ascribed to loss of moisture, surface functional groups, and guest species as well as the eventual collapse of the MOF structure as the temperature increases. The thermogram of Fe_3O_4@MIL-100(Fe)-Au (blue curve) showed an estimated weight loss of 32.40%, an indication of the successful deposition of Au on the magnetic core-shell. Besides, the relative weight loss exhibited by Fe_3O_4@MIL-100(Fe)-Au as compared to Fe_3O_4@MIL-100(Fe) shows the synergistic effect of the components on the thermal stability of the composite.

The adsorptive potential of the composite was explored by applying the nanostirrer for a biomedical application (bacteria capture). As mentioned above, the separation of analytes of interest is always conducted from biological samples with trace amounts. The solution volume for bacteria capture was set as 500 μL, which is almost unable to accommodate conventional-sized stirrers. Fe_3O_4@MIL-100(Fe)-Au was conjugated with salmonella antibody as shown in Fig. 4a. The magnetic property was subsequently harnessed on a magnetic field for the targeted capture of salmonella pathogen as illustrated in Fig. 4b. The synergy between the magnetic property and the relatively large surface area is crucial for bacteria adsorption. Whiles the Fe_3O_4 serves as the source of the magnetic property, the MIL-100(Fe)

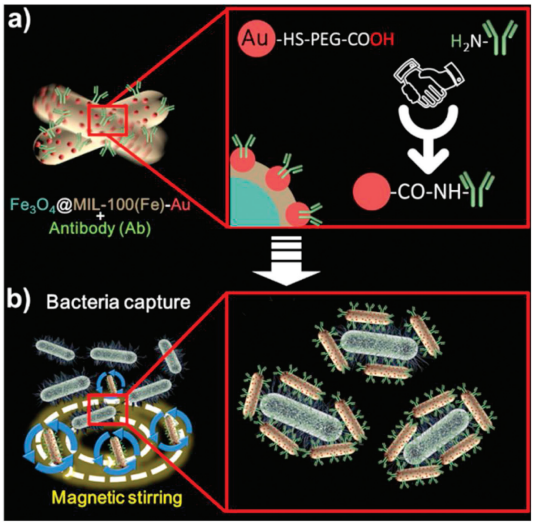

Fig. 4. Schematic illustration of (a) Conjugation of Fe_3O_4@MIL-100(Fe)-Au with antibody (Ab). (b) Magnetic field-assisted capture of bacteria pathogen.

provides adequate surface area and by conjugating the composite with specific antibodies, the specific capture of Salmonella is accomplished in an antigen-antibody specific recognition fashion. However, because the modified composite is non-polar and the solution containing the bacteria is polar, effective contact is limited resulting in reduced binding efficiency. However, with the introduction of the magnetic field, the modified composite rotates thereby increasing the contact area between the antibody and bacteria consequently leading to enhanced bacteria capture rate.

As exhibited in the TEM and HAADF- STEM and mapping overlay images (Figs. 5a–c), the elemental mapping results of the composite for bacteria adsorption as presented in Figs. 5d–f and h confirm the presence of C, Fe, Au and O, the major elemental compositions of the adsorbent as previously shown (Figs. 2e and f). In addition, the presence of N (Fig. 5g) is due to the treatment/modification of the nanostirrer with EDC and NHS for bacteria adsorption. As shown in Fig. 5i, the fluorescence intensity of magnetic field-assisted bacteria adsorption is more pronounced than the non-magnetic field-assisted adsorption, an indication of enhanced bacteria adsorption for the former than the latter. The calculated average bacteria capture rate was 58.6% and 32.9% for magnetic field-assisted adsorption and non-magnetic field-assisted adsorption respectively as illustrated in Fig. 5j. The effect of the magnetic field on bacteria adsorption was elucidated from the fluorescence field and bright field microscopy images as shown in Fig. 5k.

The observed adsorption on the magnetic field had more fluorescence, an indication of enhanced adsorption for the magnetic field-assisted system. These observations affirm that Fe_3O_4@MIL-100(Fe)-Au functions creditably as a nanoadsorbent in the elimination of biological pollutants- bacteria pathogen. Furthermore, the superior performance of the as-prepared composite as a nanoadsorbent for magnetic field-assisted capture of pathogens is a clear indication of the positive impact of the magnetic property of the composite on adsorption. Based on the obtained results, we posit that such a nanoadsorbent system can be replicated for the sequestration of other biological pollutants.

Besides the adsorption of biological contaminants, the prepared composite also exhibited a peroxidase mimetic activity and hence was deployed as a nanozyme for the colorimetric detection of H_2O_2. Although H_2O_2 has many beneficial uses in the food processing industry, the pharmaceutical industry, and in environmental fields, it is a by-product of metabolic oxidation processes [26] and immediately poses danger to life and health when concentrations are above 75 ppm [27]. The detection of H_2O_2 is therefore of prime importance. The synergy between Fe_3O_4, Fe-based-MOF and Au endows the nanostirrer with peroxidase-like properties [28–30]. The oxidation of the colorless tetramethylbenzidine (TMB) to blue by H_2O_2 after incubation for

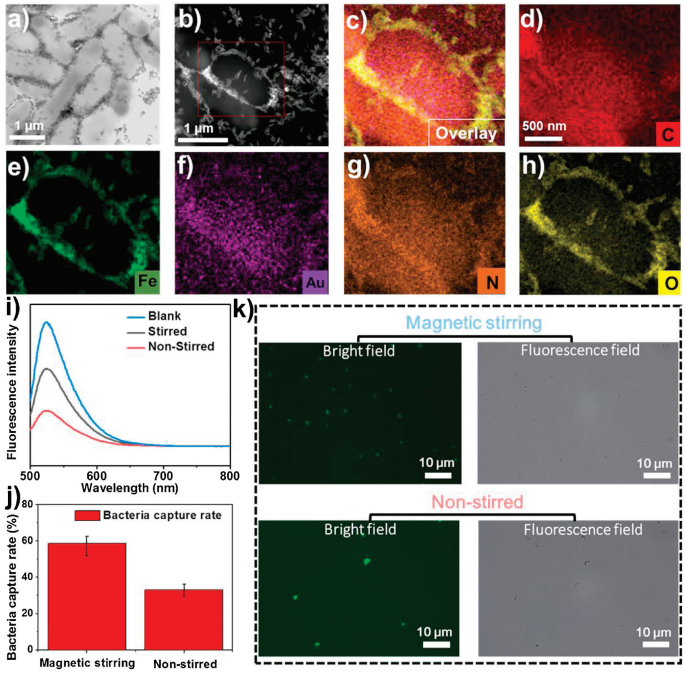

Fig. 5. (a)TEM image of adsorbed bacteria on Fe_3O_4@MIL-100(Fe)-Au. (b) STEM-HAADF image of adsorbed bacteria on Fe_3O_4@MIL-100(Fe)-Au. EDX elemental scanning and mapping. (c) Overlay maps of elements in Fe_3O_4@MIL-100(Fe)-Au, (d) carbon, (e) iron, (f) gold, (g) nitrogen and (h) oxygen. (i) Graphical presentation of the fluorescence intensity of adsorbed bacteria. (j) Graphical presentation of the mean bacteria capture rate for both magnetic field-assisted and non-magnetic field-assisted bacteria adsorption. (k) Fluorescence filed and bright field microscopy images of Salmonella captured by Fe_3O_4@MIL-100(Fe)-Au-Ab on both magnetic field and non-magnetic field.

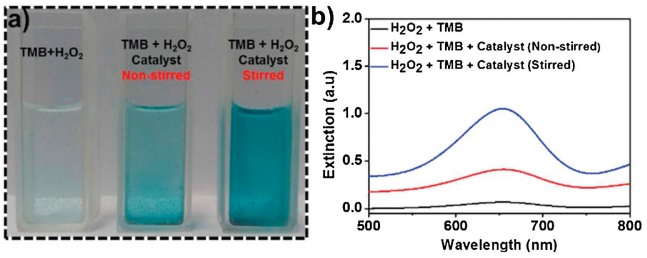

Fig. 6. (a) Picture of TMB + H_2O_2 (left), TMB + H_2O_2 + Nanozyme (middle), and TMB + H_2O_2 + Nanozyme (on magnetic field) (right). (b) UV–vis spectra for TMB oxidation with H_2O_2 without nanozyme (black), with nanozyme (non-stirred) (red), and with nanozyme (stirred) on a magnetic field (blue).

3 min is very slow (no obvious color change is observed) as evidenced in Fig. 6a. However, upon the addition of the nanozyme, pale blue color is observed after the same incubation period. The decomposition of H_2O_2 generates hydroxyl radical which oxidizes TMB to form a colored product in the presence of Fe_3O_4@MIL-100 (Fe)-Au (peroxidase). An intense deep blue color was observed when the nanozyme was applied to the reaction mixture on a magnetic field for the same duration of incubation. The observed change in coloration is due to the enhanced kinetics as a result of the stirring effect of the nanozyme on the magnetic field. As confirmed by the associated UV–vis spectra, the magnetic property of the nanozyme has been exploited to enhance the colorimetric detection of H_2O_2 (Fig. 6b). By dint of this observation, the composite has plausible potential applications as a nanosensor in similar systems.

The versatility of the prepared composite was demonstrated by applying it for the reduction of selected organic pollutants. The catalytic activity of the synthesized composite was ascertained *via* 4-NP reduction with $NaBH_4$ at the presence of the prepared catalyst. The progress of the reaction was monitored by a time-dependent UV–vis absorption spectroscopy and the necessary kinetic parameters were accordingly determined from the absorption spectra. Typically, 4-NP solution has a pale-yellow color and a characteristic absorption peak at 317 nm. Upon the addition of $NaBH_4$ solution, a conspicuous sharp yellow colored solution is formed, an indication of the formation of nitrophenolate (4-NPh) anions in the alkaline medium. Meanwhile, the characteristic absorption peak in the UV visible region shifts to 400 nm (Fig. S4a in Supporting information), thus affirming the formation of 4-NPh [31]. However, the chemical transformation of 4-NP by $NaBH_4$ does not proceed to the formation of 4-AP in the absence of

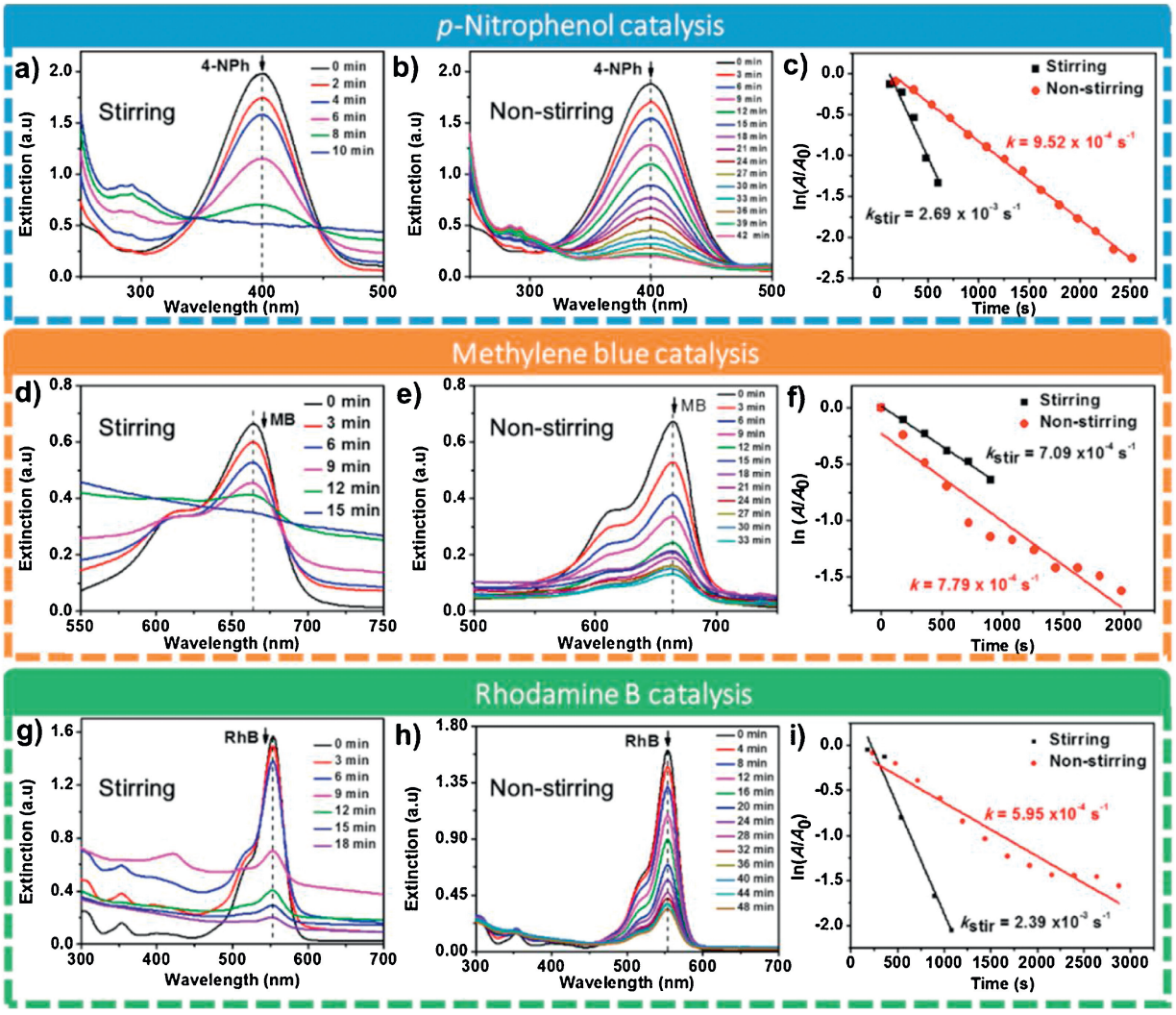

Fig. 7. Ultraviolet-visible spectra for Magnetic field-assisted catalytic reduction of (a) 4-NP, (d) MB and (g) RhB. Ultraviolet-visible spectra for non-magnetic field-assisted catalytic reduction of (b) 4-NP, (e) MB and (h) RhB. A plot of $\ln(A/A_0)$ *versus* time for the evaluation of rate constant for both magnetic and non-magnetic field-assisted catalytic reduction of (c) 4-NP, (f) MB and (i) RhB.

an efficient catalyst after a reasonable period as demonstrated in Fig. S4b (Supporting information). The introduction of Fe_3O_4@MIL-100(Fe)-Au into the reaction system results in a gradual decrease in the 4-NPh peak (400 nm) as the reaction proceeds with time. A new peak appears at 300 nm and increases as the peak at 400 nm decreases, an indication of the formation of 4-AP. The isosbestic points at 275 nm and 318 nm (Figs. 7a and b) allude to the fact that only one product, 4-AP is formed by the catalytic reduction of 4-NP at the presence of excess $NaBH_4$ [32].

The role of the magnetic property of the catalyst in enhancing catalysis was elucidated by comparing 4-NP reduction by $NaBH_4$ at the presence of the as-synthesized catalyst with and without magnetic field assistance (Figs. 7a and b). The magnetic field-assisted catalytic reaction goes into completion in less than 10 min whiles the non-magnetic field-assisted catalysis takes some 42 min to complete. The faster kinetics for the former is due to the fact that the magnetic property of the catalyst is harnessed as a stirrer on the magnetic field. The stirring effect of the composite in the reaction mixture under the magnetic field is presented in the video in the Supporting information (Video S1). Generally, stirring (agitation) is one of the major factors that impact positively on the rate of a chemical reaction. The stirring effect in the reaction medium exposes more reactant molecules to collide resulting in a greater frequency of collision and hence the effective collisions increase consequently leading to an increase in the rate of reaction as observed.

The mechanism for the synergistically enhanced activity of the composite for the conversion of 4-NP to 4-AP takes place in three major steps. The first stage involves the adsorption of 4-nitrophenolate on the surface of the catalyst *via* π-π stacking interactions between the aromatic rings of 4-NP and the organic part of the framework. Such adsorption gives rise to a local high concentration of 4-nitrophenolate near the interface of the Au and MIL-100(Fe) components, leading to an increase in contact probability and consequently effective contact between them. At the second stage, there is electron transfer from the borohydride anion to the catalyst and subsequently transferred to the 4-nitrophenolate adsorbed on the catalyst. Next, the transfer of hydrogen from the borohydride anion to 4-NP results in the formation of 4-AP. Finally, the product (4-AP) desorbs from the surface of the catalyst into solution [33,34].

The kinetic evaluation was carried out to determine the rate constant for the catalytic reduction reactions. From heuristics, since the concentration of the reductant, $NaBH_4$ (0.2 mol/L) far exceeds the concentration of 4-NP (0.18 mmol/L), the reaction rate kinetics can be considered a *pseudo*-first-order and hence the rate can be defined by (Eq. 1) [31,35]:

$$r = \ln(C_t/C_0) = \ln(A/A_0) = -kt \quad (1)$$

where r is the rate of reduction, C_t is the concentration of 4-NPh ions at time t; C_0 is the initial concentration of 4-NPh ions; $A$is the absorbance at time t; A_0 is the absorbance at time $t = 0$ and k is the rate constant which is estimated from the slope of a plot of $\ln(A/A_0)$ *versus t*. This determination was done for both magnetic field-assisted catalysis and non-magnetic field-assisted catalysis. The catalytic rate constant as per the reaction conditions for first-order kinetics for the degradation of 4-NP was estimated from the slope of the plot of ln (A/A_0) *versus* time. The rate constant, k_{stir}, for the magnetic field-assisted catalysis was 2.69×10^{-3} s^{-1}, an indication of significantly better catalytic performance than the non-magnetic field-assisted catalysis which had a rate constant, k of 9.52×10^{-4} s^{-1} as shown in Fig. 7c. To quantitatively compare different catalysts, an activity parameter is usually defined [36]. In the present study, the activity parameter, K, defined as the ratio of the apparent rate constant to the total amount of Au (mol) added to the reaction system ($K = k/n_{Au}$) was adopted [37]. The Au content of the catalyst was determined by ICP-MS and found to be 0.56%. In comparison with similar magnetic Au-based catalysts for 4-NP reduction as shown in Table S1 (Supporting information), the obtained activity parameter for both magnetic field-assisted reduction (2.4×10^4) and non-magnetic field-assisted reduction (8.4×10^3) is indicative of an excellent catalytic activity of the composite toward the degradation of 4-NP.

The composition of the catalyst is crucial in obtaining the desired optimum results for the catalysis as observed above. To highlight the synergistic effect of the resultant composite for enhancing catalysis, the individual components of the composite, Fe_3O_4 nanorod and Fe_3O_4@MIL-100(Fe) were similarly applied for the catalysis of 4-NP (as control experiments). The application of only Fe_3O_4 nanorod as a catalyst for 4-NP reduction at the presence of $NaBH_4$ had a negligible impact on the catalytic performance for both magnetic field-assisted and non-magnetic field-assisted systems as shown in Figs. S4c–e (Supporting information). Similarly, the application of Fe_3O_4@MIL-100(Fe) as a catalyst for reduction does not produce significant results for both magnetic field-assisted catalysis and non-magnetic field-assisted catalysis as exhibited in Figs. S4f–h (Supporting information). These observations (negligible catalytic activity due to the paltry rate constants) for the application of Fe_3O_4 nanorod and Fe_3O_4@MIL-100(Fe) as catalyst underscore the important role of the active ingredient, Au in the synthesized composite, Fe_3O_4@MIL-100(Fe)-Au in achieving the desired catalytic results. The MOF provides the needed surface area for accommodating the active ingredient while the Fe_3O_4 solely accounts for the magnetic property.

Catalyst reusability, an important parameter in determining the commercial viability was explored [37]. The applied catalyst in the reduction reaction was easily collected at the end of the reaction with an external magnet, rinsed with deionized water, and reapplied for the next run of reaction. The reusability test for magnetic field-assisted catalysis shows that the catalyst is stable and can be used for five successive runs without any significant loss in its catalytic ability (Fig. S5a in Supporting information).

To further corroborate the catalytic prowess of the synthesized composite and espouse the role of the magnetic property in enhancing catalysis, two other environmental pollutants, MB and RhB were explored for catalytic reduction at the presence of $NaBH_4$. The changes in the characteristic absorption peak of MB (664 nm) and RhB (553 nm) were monitored to determine the kinetic rate constant for magnetic field-assisted and non-magnetic field-assisted catalysis. Under the experimental conditions, the physical adsorption of MB dye by Fe_3O_4@MIL-100(Fe)-Au had a negligible effect on catalysis (Fig. S6a in Supporting information). Similarly, the physical adsorption of RhB by Fe_3O_4@MIL-100(Fe)-Au for both magnetic field and non-magnetic field-assisted adsorption had a negligible effect on the catalytic reduction (Fig. S6b in Supporting information). However, as shown in Figs. 7d–f, the reduction of MB by $NaBH_4$ at the presence of the catalyst is relatively fast as evidenced by the rapid disappearance of the characteristic absorption peak of MB at 664 nm. Besides, the performance of magnetic field-assisted reduction of MB is enhanced in comparison with non-magnetic field-assisted reduction. Similarly, the trend of results for the reduction of RhB dye was not different from the former as shown in Figs. 7g–i. A graphical illustration of the comparison of both magnetic field-assisted and non-magnetic field-assisted reduction of the selected pollutants is presented in Fig. S5b (Supporting information). Clearly, from the foregoing analysis, it is evident that the magnetic property of the catalyst can further enhance catalysis.

In summary, Fe_3O_4@MIL-100(Fe)-Au was prepared from magnetic Fe_3O_4 nanorods, MIL-100(Fe), and Au. The characterization of the composite by TEM, XRD, EDX, FTIR, UV–vis, VSM, TGA gives credence to the formation of the composite. Not only does the prepared composite function as nanoadsorbent-cum-catalyst but also as a nanostirrer. The magnetic property of the Fe_3O_4@MIL-100 (Fe)-Au was successfully harnessed to sequester bacteria pathogen from solution, to enhance the colorimetric detection of H_2O_2, and to enhance the reduction of the organic pollutants, 4-NP, MB, and RhB. Furthermore, the multifunctional composite can conveniently be separated from the reaction stream using an external magnet and reapplied for successive runs as demonstrated for 4-NP reduction. The espoused magnetic field-assisted approach has great prospects in the future. It is adaptable for microscale and nanoscale reaction systems such as lab-on-chip applications where conventional stirrers are not applicable. Not only will such applications decrease the risk associated with external stirrer-pollutants in reactions but also help to safely execute important researches involving dangerous and explosive chemicals by dint of the controllable volume of reactants involved.

Declaration of competing interest

The authors declare no conflict of interest.

Acknowledgments

This work was financially supported by the National Natural Science Foundation of China (No. 21876206), the Science and Technolgy Projects of Qingdao (No. 21-1-4-sf-7-nsh), the National Key Technologies R&D Program of China, Key Projects of Intergovernmental International Innovation Cooperation (No. 2018YFE0118200) and the Shandong Key Research and Development Project (Nos. 2019JZZY010506, ZR2020ZD13).

Appendix A. Supplementary data

Supplementary data associated with this article can be found, in the online version, at https://doi.org/10.1016/j.cclet.2021.03.019.

References

[1] A. Kirchon, L. Feng, H.F. Drake, E.A. Joseph, H.C. Zhou, Chem. Soc. Rev. 47 (2018) 8611–8638.
[2] L. Xu, M. Pan, G. Fang, S. Wang, Sens. Actuators B: Chem. 286 (2019) 321–327.
[3] X. Wang, K. Li, J. He, et al., Nano Energy 78 (2020) 105388.
[4] L. Yan, A. Amirshaghaghi, D. Huang, et al., Adv. Funct. Mater. 28 (2018) 1–8.
[5] H.L. Chee, C.R.R. Gan, M. Ng, et al., ACS Nano 12 (2018) 6480–6491.
[6] B.E. Meteku, J. Huang, J. Zeng, et al., Coord. Chem. Rev. 413 (2020) 213261.
[7] H. Alamri, A. Al-Shahrani, E. Bovero, T. Khaldi, et al., J. Colloid Interface Sci. 513 (2018) 349–356.
[8] J. Mohapatra, A. Mitra, H. Tyagi, D. Bahadur, M. Aslam, Nanoscale 7 (2015) 9174–9184.
[9] L. Heinke, C. Wöll, Adv. Mater. 31 (2019) 1806324.
[10] Y.S. Kang, Y. Lu, K. Chen, et al., Coord. Chem. Rev. 378 (2019) 262–280.
[11] R.B. Lin, S. Xiang, H. Xing, W. Zhou, B. Chen, Coord. Chem. Rev. 378 (2019) 87–103.
[12] S. Wang, Y. Chen, S. Wang, et al., J. Am. Chem. Soc. 141 (2019) 2215–2219.
[13] Z. Li, J. Hu, Y. Xiao, et al., Anal. Chim. Acta 1146 (2021) 174–183.
[14] P. Mishra, S. Patnaik, K. Parida, Catal. Sci. Technol. 9 (2019) 916–941.
[15] P. Falcaro, R. Ricco, A. Yazdi, et al., Coord. Chem. Rev. 307 (2016) 237–254.
[16] K. Kuśmierek, A. Witkowski, React. Kinet. Mech. Catal. 116 (2015) 261–271.
[17] S. Yang, C. Cao, Y. Sun, et al., Angew. Chem. Int. Ed. 54 (2015) 2661–2664.
[18] Y. Liu, J. Zhang, X. Zhang, et al., J. Mater. Chem. A 4 (2016) 4280–4287.
[19] E.O. Pentsak, D.B. Eremin, E.G. Gordeev, V.P. Ananikov, ACS Catal. 9 (2019) 3070–3081.
[20] C. Vollmer, M. Schröder, Y. Thomann, R. Thomann, C. Janiak, Appl. Catal. A: Gen. 425–426 (2012) 178–183.
[21] J.M. Thomas, K.D.M. Harris, Energy Environ. Sci. 9 (2016) 687–708.
[22] W. Xu, M. Wang, Z. Li, et al., Nano Lett. 17 (2017) 2713–2718.
[23] S. Aslam, J. Zeng, F. Subhan, et al., J. Colloid Interface Sci. 505 (2017) 186–195.
[24] S. Li, J. Cui, X. Wu, et al., J. Hazard. Mater. 100 (2019) 408–416.
[25] H.J. Zhang, S. Da Qi, X.Y. Niu, et al., Catal. Sci. Technol. 4 (2014) 3013–3024.
[26] A. Chen, S. Chatterjee, Chem. Soc. Rev. 42 (2013) 5425–5438.
[27] J. Sun, C. Li, Y. Qi, S. Guo, X. Liang, Sensors. 16 (2016) 584.
[28] L. Gao, J. Zhuang, L. Nie, et al., Nat. Nanotechnol. 2 (2007) 577–583.
[29] A. Liu, M. Li, J. Wang, et al., Chin. Chem. Lett. 31 (2020) 1133–1136.
[30] J. Chen, H. Gao, Z. Li, Y. Li, Q. Yuan, Chin. Chem. Lett. 31 (2020) 1398–1401.
[31] T. Aydan, C. Yang, Y. Xu, et al., Inorg. Chem. Commun. 102 (2019) 162–170.
[32] P. Hervés, M. Pérez-Lorenzo, L.M. Liz-Marzán, et al., Chem. Soc. Rev. 41 (2012) 5577–5587.
[33] F. Ke, L. Wang, J. Zhu, Nanoscale 7 (2015) 1201–1208.
[34] A.A. Kassem, H.N. Abdelhamid, D.M. Fouad, S.A. Ibrahim, J. Environ. Chem. Eng. 9 (2021)104401.
[35] S.R. Thawarkar, B. Thombare, B.S. Munde, N.D. Khupse, RSC Adv. 8 (2018) 38384–38390.
[36] Z. Dong, X. Le, Y. Liu, C. Dong, J. Ma, J. Mater. Chem. A 2 (2014) 18775–18785.
[37] Y. Xu, X. Shi, R. Hua, et al., Appl. Catal. B: Environ. 260 (2020) 118142.